Alcator C-Mod Soft X-Ray Pulse Height Analysis System

by

Eliseo Gamboa

Submitted to the Department of Physics
in partial fulfillment of the requirements for the degree of

Bachelor of Science in Physics

at the

MASSACHUSETTS INSTITUTE OF TECHNOLOGY

June 2007

© Massachusetts Institute of Technology 2007. All rights reserved.

Author . . . .
Department of Physics
May 18, 2007

Certified by. . . . .
John E. Rice
Principal Research Scientist, Alcator Project
Thesis Supervisor

Accepted by . . . .
Professor David E. Pritchard
Senior Thesis Coordinator, Department of Physics

Alcator C-Mod Soft X-Ray Pulse Height Analysis System

by

Eliseo Gamboa

Abstract

A pulse height analysis (PHA) system has been installed on the Alcator C-Mod magnetic confinement fusion experiment. The PHA utilizes a Si(Li) detector to measure soft X-rays in the 1-30 keV range with an energy resolution on the order of 100eV. A FASTComtec MCA-3 multichannel analyzer allows integration times of 1ms while the PHA supports counting rates of up to 80kHz. The thermal electron temperature is measured from the energy dependence of the intensity of the electron bremsstrahlung spectrum. Measurements of line radiation allows the PHA to identify impurity ions within each plasma shot. The result is a diagnostic that measures thermal electron temperatures while aiding in the indentification of heavy ($Z¿12$) impurities.

Thesis Supervisor: John E. Rice
Title: Principal Research Scientist, Alcator Project

Acknowledgments

I would like to foremost thank everyone at the MIT PSFC. I am indebted to my thesis suprevisor John Rice and the invaluable tutelage of Matt Reinke. I would also like to thank Alex Ince-Cushman, Yuri Podpaly, Tom Toland, Earl Marmar, Bruno Coppi, and Francesca Bombarda.

Contents

Chapter 1

Introduction

Creating new and alternative energy sources to meet the ever-growing global demand is one of the most difficult problems facing scientists and engineers today. Ever since crude coal fired power plants blackened 19th century cities, new technologies have emerged that have made electricity production cleaner and more efficient. Nevertheless, it seems that power production through conventional fossil fuel based technologies will never be sustainable. Creating power through nuclear fusion holds the promise of yielding a clean and nearly inexhaustible source of power through manipulating the same reactions that sustain the sun. Realizing this goal is not without challenge as scientists all over the world have strived to create energy through fusion for over fifty years.

The technique of magnetic confinement fusion studied in the Alcator C-Mod experiment holds the best chance of realizing net power production. This paper details the development of a new soft x-ray diagnostic in C-Mod to study the behavior of electrons and impurity ions in the plasma. The overall goal is to utilize advances in computerized signal processing elements to give researchers a between shot measurement of the emissivity of the plasma in the energy range of 1 to 30 keV.

The first chapter gives some background to the development and implications of nuclear fusion power. It then goes on to describe the operating goals of the PHA. The second chapter gives a theoretical model of the emissivity of the plasma in the soft x-ray range and considers the appropriate approximations based on the limi-

tations of the detector. The third chapter presents the PHA hardware along with calibrations and limitations of the system. Chapter four gives some sample spectra collected from plasma discharges and presents a comparision to the results from established diagnostics. Finally, possibilities for future expansions of the PHA system are discussed.

1.1   Background to Fusion Energy

While modern fossil fuel power plants are orders of magnitude cleaner than their predecessors, the finite fossil fuel supply and the environmental impact from these power stations calls into question the long term viability of energy from these sources.

The majority of power production in the United States comes from coal, widely regarded as one of the dirtiest ways to generate power. Particulates, sulfur compounds, and heavy metals emitted from coal power plants are difficult to mitigate. Scrubbers can cut this pollution, but they add to the overall cost and complexity of the power stations. While government regulations can force operators to install these systems in the United States, countries in the developing world often lack this technology or incentives to install it. In particular, China, which is undertaking a massive expansion of their electrical production capacity through building new coal power plants, is set to overtake the United States in net carbon dioxide output.

The current alternatives to fossil fuels all have their own drawbacks as well. While producing little carbon, the massive Three Gorges Dam under construction on the Yangtze in China has displaced over a million people from their homes and drastically altered the local ecology. Solar and wind power still cannot compete with the economies of scale possible through fossil fuels. Public opposition to nuclear fission power and concerns about proliferation have greatly curtailed the scale of nuclear power production. In comparison to other methods of generating power, nuclear fusion presents somewhat of an anomaly - power without appreciable carbon emissions and a fuel as common as water.

The promise of energy through fusion is evident from the energy scales involved.

The chemical reactions in fossil fuel plants release energy on the scale of a few eV per reaction. Fusion reactions typically release energy seven orders of magnitude greater. Harnessing this energy source could revolutionize the way our society treats issues of development and economic leverage.

With the construction of the next generation ITER experiment expected to begin in 2008, research in fusion is on the verge of a great breakthrough in capabilities. Barring any major catastrophes, the knowledge gained at ITER should put researchers within striking range of building the first demonstration fusion power plant.

1.2   Progress in Fusion Research

With the advances of quantum mechanics in the early 20th century, physicists were first able to describe accurately the reactions that powered the sun. Beginning in 1920, Arthur Eddington advanced the idea that nuclear reactions, not chemical processes or gravitational contraction, were responsible for the great energy source within the sun. In the late 1930, Hans Bethe worked out the details of stellar nucleosynthesis and showed that the CNO cycle and p-p chain were the mechanisms by which hydrogen in the sun's core was converted into helium.

The next great advance in early fusion research came with the development of the thermonuclear bomb. Edward Teller and Stanislaw Ulam were the chief contributers to the design of a bomb which would produce the first artificial fusion reactions. The 1951 Teller-Ulam design became the basis of future thermonuclear weapons. While fusion can be produced with relative ease through detonating a thermonuclear weapon, creating and maintaining the extreme temperatures and densities necessary to produce fusion reactions are very difficult to do in a controlled manner.

The earliest efforts at creating a controlled nuclear fusion reaction centered on toroidal devices using electric currents to generate magnetic fields. Pinch devices dominated early research, but the inherent instabilities of these configurations presented a major hurdle to progress. These early efforts were also constrained by the reality of the Cold War. Fusion power research was kept under close secrecy as it was
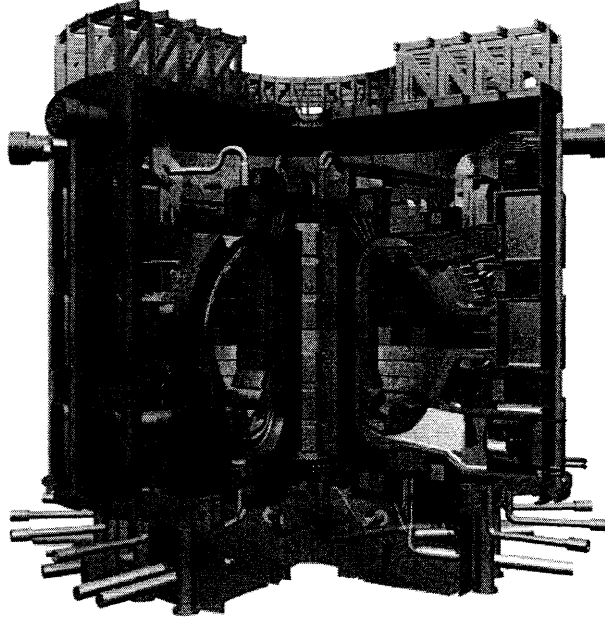
Figure 1-1: Cutaway of ITER device (published with permission of ITER)

largely a derivative of weapons research and itself a strategic asset.

Starting in 1958, the secrecy behind fusion research was lifted and a global effort towards realizing controlled nuclear fusion began to form. In 1968, Andrei Sakharov and his team unveiled the T-3 fusion experiment to the world. The novel device was based on a tokamak and had operating parameters far and above any other experiment in the world. Mainstream fusion research embraced the tokamak and construction of large tokamak-based fusion experiments began around the world in the 1970s.

In 1975, the Alcator A experiment began operation in the MIT Francis Bitter Magnet Laboratory. The experiment was conceived as a compact, high-field torus able to probe plasmas at densities and temperatures out of the reach of the reach of larger experiments. The facility was upgraded and in 1982 Alcator C went online. Finally, the latest iteration, Alcator C-Mod began operation in 1993.

In 1985, the European Union, United States, Soviet Union, and Japan agreed to collaborate on the construction of a next-generation fusion experiment. The experiment, dubbed ITER, underwent various political and financial difficulties over the next two decades owing to the diversity of the parties involved. The plan was finalized in November 2006 with construction to begin in 2008 and generation of the first

plasma around 2016.

1.3   The Magnetic Confinement Solution

The problem in designing a containment vessel for a fusing plasma comes from the extreme operating parameters demanded of the device. For typical fusion experiments, the containment vessels have to contain plasmas with temperatures in excess of 10 million degrees. Fortunately, plasmas lend themselves to be contained by electromagnetic forces by nature of the charges of the constituents.

The early pinch devices use a single magnetic field to confine the plasma. Powerful magnetic coils lining the chamber generate a toroidal field that pinches and guides the plasma around the torus. The critical instability in a pinch device comes from a cross drift. Inhomogeneities in the applied magnetic field and centrifugal forces act on the plasma. As the plasma particles circulate around the torus, positively charged ions will tend to drift towards the top of the device and electrons will collect on the bottom.

These instabilities can be compensated for by applying an additional magnetic field. In tokamaks, a current is introduced within the circulating plasma. This current generates an additional poloidal field. The toroidal and poloidal fields superimpose to generate a combined field that traps the plasma along helical field lines wrapping around the torus.

Since the 1970s, tokamaks have been the mainstream of research into magnetically confined fusion. Consequently the physics of tokamak confined plasmas is better understood than any other configuration. With the exception of major breakthroughs in other devices, tokamaks have the best chance of achieving power production in the near future.

1.4 Nuclear Fusion Reactions

In the simplest terms, a nuclear fusion interaction occurs when two light nuclei combine to form a heavier daughter nucleus. For this interaction to occur, the two nuclei must have sufficient initial kinetic energies to overcome the Coulombic force of repulsion from their positively charged protons.

If the nuclei can overcome the Coulombic energy barrier and come to a very close proximity, the nuclear force will dominate and pull the nuclei together forming a new atom. For light elements, the resulting atom will be in a lower energy state and thus some of the initial nuclear binding energy will be released in the form of energetic particles and photons.

Since the Coulombic repulsion is proportional to Z^2 and the strength of the nuclear forces increases with the number of nucleons, the isotopes of hydrogen are an ideal fuel for fusion reactions. Because of the low temperature and high cross section for interaction, currently the most promising fusion reaction for study is that between the two hydrogen isotopes deuterium and tritium.

$$^3_1 T + ^2_1 D \rightarrow ^4_2 He + n$$
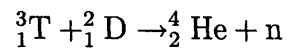
The D-T reaction produces 17.6 MeV of energy in the form of the kinetic energies of the alpha particle and neutron. While the alpha particle can be contained using electromagnetic fields, the neutron escapes the fusing plasma taking a fraction of the reaction energy with it.

For a fusing plasma to be self-sustaining, the self-heating from collisions with the energetic alphas must compensate for the energy losses from radiation, interactions with the containment vessel, and other losses. A plasma at this state is said to be ignited, no additional heating is necessary to sustain the reaction. Producing ignited plasmas is one of the end goals of fusion research as power can be produced in the steady state.

1.5 X-Ray Emissions

Critical to constructing a successful fusion experiment is understanding and managing the power radiated from plasmas by high-energy photons. If we model the plasma as a black body, the peak in intensity will come from soft x-rays. Measuring this emission can yield information on the temperature and composition of the plasma.

The PHA diagnostic I have developed uses a high-range, low-resolution solid state detector to measure the soft x-ray spectrum from plasmas in C-Mod. While the Si(Li) detector used in the PHA system lacks the fine resolution of diffractometers, the modest resolution allows the detector to monitor emission over a large energy range.

PHA systems using solid-state detectors are nothing new to the Alcator experiment. Some of the first work with PHA systems in Alcator was done by Rice et. al.on Alcator A [1] and later on Alcator C [2]. Similar system are in use at JET [3], HT-7 [4], and nearly every other tokamak experiment.

The strength of the current PHA system lies in the use of modern computerized signal processing equipment, particularly the FastComtec MCA-3 multichannel analyzer, paired with a software interface developed to automate data acquisition and analysis. The new PHA system is a diagnostic that trades energy resolution for range to give an overall description of soft x-ray radiation from plasma discharges. Fast signal processing allows the PHA to operate continuously in real time across entire plasma discharges.

1.5.1 Measurement Goals

The PHA system has two overall goal from measurements of the emissions in the soft x-ray spectrum from 1 - 30 keV.

The first goal is to measure bremsstrahlung radiation from the interaction of free electrons and ions in the plasma. Analysis of the bremsstrahlung spectra will give a measure of the thermal electron temperature. This measurement will act as a comparison to the values from established temperature measurements from electron

cyclotron radiation and Thomson scattering.

The second primary goal is to investigate the soft x-ray spectra from bound electrons in ionized impurities within the plasma. While the resolution of the detector is not sufficient to resolve the charge states of individual emitters, it will permit easy identification of impurity species over a broad range of energies.

Time integration of the data collection will allow determination of when the plasma takes on each impurity. Comparing these values to the measured electron temperature across different plasmas will yield information on the temperature dependence of the relative impurity emission rates.

The full spectrum from each discharge will give a measure of the relative abundance of impurity species relative to baseline values. For a variety of different plasma operating regimes a comparison will be done of the recorded impurity content and electron temperature.

An additional goal comes in the detection of plasma collision with the containment vessel. This will manifest itself as a sudden increase in the line strength of impurities that make up the plasma facing components. The PHA system will support the detection of these collisions.

Chapter 2

Soft X-Ray Emission

A theoretical description of the emission of soft x-rays in the 1-30 keV range can be broken into three broad categories depending on the final and initial states of the electrons. Free-free and free-bound electron radiation make up a radiation continuum while bound-bound transitions manifest themselves as discrete line emissions. The continuum radiation and line emissions will be treated seperately.

2.1   Continuum Electron Radiation

At temperatures above a few eV, the deuterium fuel inside the containment vessels is ionized. As we go higher in temperature towards the few keV in C-Mod, impurities within the plasma will ionize as well. We may divide the constituents of the plasma into a few broad categories. The main component of the plasma is the ionized deuterium fuel. This ionization gives rise to two majority populations, the deuterium nuclei and a collection of free electrons. In addition to the deuterium, there is also a very small population of alpha particles from fusion reactions.

Understanding the behavior of electrons in the plasma is of key importance to a successful fusion experiment. In particular, we may measure the interactions of free electrons with impurities to yield information about the plasma. Radiative free electron interactions with impurities occur through two primary methods. An incoming electron may collide and scatter off an ion, emitting a photon in the process. This

free-free electron interaction is known as bremsstrahlung radiation. Similarly, an initially free electron may collide with an impurity and enter into a bound state. The radiation emitted from free-bound interactions of this type is called recombination radiation.

For the range of x-ray energies visible through the detector, the bremsstrahlung and recombination radiation will come from a population of thermal electrons. The intensity of the bremsstrahlung spectrum will be dependent on the electron temperature. The overall goal from the measurement of free-electron radiation will be to arrive at a value for the electron temperature.

2.1.1 Bremsstrahlung Radiation

When a free electron collides and scatters off a positively charged ion, the electron will undergo a deflection from its initial course. In the deflection the electron experiences an acceleration. That acceleration causes the electron to emit radiation. This characteristic bremsstrahlung radiation forms a continuum with the energy of the emitted photon dependent on the initial energy of the electron, impact parameter of the collision, and the charge of the ion

For a first approximation, we may treat the problem classically as a two body collision. We have an electron with impact parameter b and initial velocity v_0 scattering off the Coloumbic potential of an ion of mass M and charge $+Ze$. Two unbound orbits are possible, a parabolic orbit and a hyperbolic orbit. The path of the electron is described by the orbit equation as

$$r(\theta) = \frac{4\pi\epsilon_0 m_e v_0^2 b^2}{Ze^2(1 + \epsilon\cos\theta)} \qquad (2.1)$$

where ϵ is the eccentricity given as

$$\epsilon = \sqrt{1 + \frac{4\pi\epsilon_0 m v_0^2 b}{Ze^2}}$$

18

and conservation of energy yields the relation

$$1/2mv_0^2 = 1/2m\dot{r}^2 + 1/2mr(\dot{\theta})^2 - \frac{Ze^2}{4\pi\epsilon_0 r}. \tag{2.2}$$

Taking the interaction as a two body system suggests we use the dipole radiation formula to get the radiated power. If we calculate the acceleration of the electron from the orbit equation, we may then easily arrive at the dipole radiation spectrum [5].

$$\frac{dE}{d\omega/2\pi} = \frac{4}{3c^3}\frac{e^2}{4\pi\epsilon_0}d^2|\ddot{r}(\omega)|^2, \tag{2.3}$$

$$d = \mu(\frac{e}{m_e} - \frac{Ze}{M}),$$

Here d is the non-dimensional strength of the electric dipole and μ is the reduced mass of the electron-ion system.

Following [6], we can express $\ddot{r}(\omega)$ as a Fourier transform of the acceleration $\ddot{r}(t)$ of the electron as described in our expressions for energy conservation and the orbit equation. Solving the differential equation for $\dot{r}$ given in 2.2 using 2.1 and differentiating yields an expression for $\ddot{r}(t)$. Performing the Fourier transform on $\ddot{r}(t)$ and substituting this expression into (2.3) gives the following

$$\frac{dE}{d\nu} = \frac{4}{3c^3}\frac{e^2}{4\pi\epsilon_0}d^2\left|\int_{-\infty}^{\infty}\ddot{r}(t)e^{\imath\omega t}dt\right|^2, \tag{2.4}$$

Finally, to find the total power emitted per unit frequency per volume for an electron to interact with a collection of ions of density n_i, we must multiply the above expression by $n_i v_1$. Integrating over all values of the impact parameter gives the following expression for the power spectrum

$$\frac{dP}{d\nu} = \frac{4n_i v_0}{c^3}\frac{e^2}{4\pi\epsilon_0}d^2\int_0^{\infty}2\pi b db\left|\int_{-\infty}^{\infty}\ddot{r}(t)e^{\imath\omega t}dt\right|^2 \tag{2.5}$$

Evaluating these integrals gives a formula for the classical bremsstrahlung energy spectrum which was first derived by Kramers [7]. In terms of Hankel functions of the

19

first kind, the full expression for the bremsstrahlung radiated power is

$$\frac{dP}{d\nu} = \frac{2Z^2\pi^2 n_i d^2}{3c^3 v_0} \left(\frac{e^2}{4\pi\epsilon_0}\right)^3 \nu_0 \left|H^{(1)}_{\imath\nu_0}(\imath\nu_0)\right| \dot{H}^{(1)}_{\imath\nu_0}(\imath\nu_0) \tag{2.6}$$

$$\nu_0 = \omega\frac{e^2}{\epsilon_0\mu v_1^3},$$

where ν_0 is a non-dimensionalized frequency. This result can be expressed for the case of an electron scattering off a stationary ion in somewhat simpler form as [6]

$$\frac{dP}{d\nu} = \frac{32\pi^2 Z^2 n_i}{3\sqrt{3}m_e^2 c^3 v_0} \left(\frac{e^2}{4\pi\epsilon_0}\right)^3 \frac{\pi\sqrt{3}}{4} u_{90}H_{u_{90}}(u_{90})\dot{H}_{u_{90}}(u_{90}), \tag{2.7}$$

$$u_{90} = \frac{i\omega b_{90}}{v_0}, b_{90} = \frac{Ze^2}{4\pi\epsilon_0 m_e v_0^2} \tag{2.8}$$

with b_{90} as the impact parameter necessary for 90° scattering and u_{90} defined analogously to ν_0. Grouping the Hankel functions together with u into a new function $G(u)$ defined as

$$G(u) = \frac{\pi\sqrt{3}}{4}H_u(u)\dot{H}_u(u) \tag{2.9}$$

we can rewrite 2.7 as

$$\frac{dP}{d\nu} = \frac{32\pi^2 Z^2 n_i}{3\sqrt{3}m_e^2 c^3 v_0} \left(\frac{e^2}{4\pi\epsilon_0}\right)^3 G(u_{90}), \tag{2.10}$$

The non-dimensional factor G(u) is called the Gaunt factor after the work of J.A. Gaunt [8]. Gaunt originally derived approximation functions to G(u) as corrections to Kramer's derivation of the bremsstrahlung power spectrum to fit observations of astronomical x-rays. However, Gaunt was unable to devise a correction that gave a full agreement between Kramer's classical derivation and observations of high-energy radiation. To arrive at a full description of bremsstrahlung radiation, we must introduce quantum mechanical corrections. These corrections are traditionally expressed as modifications to the Gaunt factor to preserve the classical limit of Kramer's derivation.

Quantum Mechanical Bremsstrahlung

The first full quantum treatment of bremsstrahlung radiation was performed by Sommerfeld and Maue in 1935 [9]. The derivation was based on two quantum numbers, η_0 and η_f, representing the initial and final energy states of the free electron in a manner analogous to the energy states of bound electrons in the Bohr model. We may define these quantum numbers in terms of the ionization energy of hydrogen $R_y = -13.59$ eV and the frequency of the emitted radiation ν as

$$E_0 = \frac{Z^2 R_y}{\eta_0^2} = \frac{1}{2}mv_0^2, \tag{2.11}$$

$$h\nu = Z^2 R_y\left(\frac{1}{\eta_f^2} - \frac{1}{\eta_i^2}\right), \tag{2.12}$$

The quantum mechanical Gaunt factor was given in 1939 by Sommerfeld[10] in the form

$$G = \frac{\sqrt{3}\pi x}{(e^{2\pi\eta_0} - 1)(1 - e^{2\pi\eta_f})} x \frac{d}{dx}|F(x)|^2 \tag{2.13}$$

where F(x) is the ordinary hypergeometric function defined as

$$F(x) =_2 F_1(\imath\eta_0, \imath\eta_f; 1; -x) \tag{2.14}$$

$$= 1 + \eta_o\eta_f x + (\imath\eta_0 - \eta_0^2)(\imath\eta_f - \eta_f^2)\frac{x^2}{4} + ...,$$

$$x = \frac{4\eta_0\eta_f}{(\eta_f - \eta_0)^2},$$

To calculate the emissivity of the bremsstrahlung radiation, we return to our expression for the differential power spectrum 2.10 and integrate over an appropriate electron energy distribution. The emissivity comes from evaluating the integral

$$4\pi\epsilon(\nu)) = \int \frac{dP}{d\nu} f(v) d^3v \tag{2.15}$$

Here the emissivity is in units of power / unit frequency volume solid angle. Continuum radiation in the soft x-ray range in Alcator has been observed from elec-

tron bremsstrahlung radiation[1]. Taking the electron energies to follow a Maxwell-Boltzmann distribution and integrating over the initial electron velocity v_0 we have

$$4\pi\epsilon(\nu) = A \int_0^\infty \sqrt{\frac{m_e}{2\pi kT}} \frac{G(\nu, v_0)}{v_0} e^{-mv_0^2/2kT} 4\pi v_0^2 dv_0 \tag{2.16}$$

$$A = \frac{32\pi^2 Z^2 n_i}{3\sqrt{3}m_e^2 c^3 v_0} \left(\frac{e^2}{4\pi\epsilon_0}\right)^3 \tag{2.17}$$

Where I have grouped all the constants into a factor A with units of power per unit frequency. Rewriting the integral in terms of $E_0 = 1/2mv_0^2$ yields [6]

$$\epsilon(\nu) = \frac{A}{4\pi} n_e \sqrt{\frac{m_e}{2\pi kT}} \int_{h\nu}^\infty G(\nu, v) e^{-E_0/kT} \frac{dE_0}{kT} \tag{2.18}$$

$$\tag{2.19}$$

Using 2.11 and 2.12, we may rewrite the integral in the above expression in terms of of the final electron energy

$$g_{ff} = e^{-h\nu/kT} \int_0^\infty G(\nu, E_f + h\nu) e^{-E_f/kT} \frac{dE_f}{kT} \tag{2.20}$$

This quantity g_{ff} is called the Gaunt factor for free-free emission. This represents the quantum mechanical correction for free-free electron interactions. Rewriting the total bremsstrahlung power per unit frequency given in 2.16 in terms of this new factor, we have

$$\epsilon(\nu) = \frac{8\pi Z^2 n_i n_e}{3\sqrt{3}m_e^2 c^3} \left(\frac{e^2}{4\pi\epsilon_0}\right)^3 \sqrt{\frac{m}{2\pi kT}} e^{-h\nu/kT} g_{ff} \tag{2.21}$$

This expression gives the total bremsstrahlung power emitted from thermal electrons in a Maxwellian plasma interacting with a single impurity species in terms of the ion and electron densities, the plasma temperature, and the Gaunt factor for free-free emission.

Even though we have an expression for the intensity of the emitted radiation in closed form in 2.21, the presence of the hypergeometric function in g_{ff} makes this expression difficult to use in practice. Fortunately, we can use an approximation in

place of the free-free Gaunt factor. For the range of x-ray energies likely to be seen by the detector, replacing g_{ff} by $(h\nu/kT)^{\frac{1}{3}}$ gives a very good approximation [1].

Observation of the bremsstrahlung spectrum from plasmas yields a continuum spectrum with discontinuities which our formula for continuum radiation cannot explain. A correction for recombination radiation is needed to introduce the quantized nature of the bound electron energy levels in the impurity ions.

2.1.2 Radiative Recombination

Radiative recombination is the process by which an initially free electron is captured and put into a bound state by an impurity ion. Recombination radiation was first discussed by Kramers [7] then Menzel and Pekeris[11] and expanded by Brussard and Van de Hulst[12] and then Karzas and Latter[13]. Here I present an overview of the calculation of the power spectrum from radiative recombination.

We can understand free-bound electron transitions in terms of transitions from free hyperbolic orbits into bound elliptical ones. The process releases an energy which can be expressed as

$$\Delta E = Z^2 R_y (\frac{1}{n^2} - \frac{1}{\eta_0^2}),$$ (2.22)

where n is the principle quantum number of the final bound state and η_0 is the Sommerfeld quantum number for the free electron. The electron interaction with the atom is dependent on the initial electron energy. For an electron with initial kinetic energy $E_0 = 1/2mv_0^2$, recombination is only possible if the initial energy is less than the energy of the bound state, $E_0 < Z^2 R_y\, n^2$. If the opposite is true, the electron will scatter off the ion and emit bremsstrahlung radiation.

For the case of electron recombination, we can rearrange 2.22 to give the allowed energy spectrum.

$$\Delta E = \frac{Z^2 R_y}{n^2} + E_0$$ (2.23)

or, rewriting to give the radiation spectrum, we have

$$h\nu = \frac{Z^2 R_y}{n^2} + 1/2mv_0^2, \tag{2.24}$$

The radiation spectrum will thus be a series of discrete jumps superimposed on the bremsstrahlung continuum.

Following [6], we may arrive at a semi-classical estimate of the recombination radiation by the correspondence principle. Assuming a parabolic collision, the radiation spectrum from recombination should come completely from quantized radiation. There will be no continuum, only a series of stepwise radiation bands. However, the correspondence principle tells us that at the limit of high electron energy any formula we derive for recombination radiation should reproduce the bremsstrahlung continuum. Using this reasoning, each recombination level n should quantize the bremsstrahlung continuum for some region near n. We can modify our expression for the radiation spectrum to account for this by quantizing the bremsstrahlung continuum using 2.24.

Around each level we take the condition that each discrete energy level covers some range in the continuum. The recombination energy $h\nu$ quantized by the nth level is smeared out over a range given as

$$1/2mv^2 + \frac{Z^2 R_y}{(n+1/2)^2} \le h\nu \le 1/2mv^2 + \frac{Z^2 R_y}{(n-1/2)^2}, \tag{2.25}$$

The power emitted from the capture of an initially free electron into a bound state n is then

$$P(n) = \frac{dP}{d\nu} \Delta\nu_n g_n(\nu), \tag{2.26}$$

where we use the expression given in 2.21 for $\frac{dP}{d\nu}$ in the classical limit.

$$\frac{dP}{d\nu} = A = \frac{32\pi^2 Z^2 n_i}{3\sqrt{3}m_e^2 c^3 v_0} \left(\frac{e^2}{4\pi\epsilon_0}\right)^3 \tag{2.27}$$

The quantum mechanical calculations are encapsulated in the new Gaunt factor $g_n(\nu)$. Calculations of this factor are similar to that of the free-free Gaunt factors and amount to evaluating transition dipole matrix elements with final states that are bound. Low-Z impurities present in the plasma, like carbon and oxygen, are likely to be completely ionized. For low-Z impurities, calculations of the transition dipole matrix elements are straightforward and the recombination radiation can be easily calculated. Calculations of the Gaunt factor for partially ionized heavy impurities are considerably more complex. In many cases it is easier to measure directly the radiation spectrum from partially-ionized heavy-Z impurities than calculate the emitted power from 2.26.

Using 2.25, the frequency range quantized by each level $\Delta\nu_n$ is approximately

$$\Delta\nu_n = \frac{2Z^2 R_y}{hn^3} \tag{2.28}$$

Substituting the expressions for $\Delta\nu_n$ and $\frac{dP}{d\nu}$ into 2.26 gives

$$P(n, v_0) = Ag_n(\nu)\frac{2Z^2 R_y}{hn^3} \tag{2.29}$$

This is the power emitted from recombination radiation of an electron with initial velocity v to the energy level n. To calculate the total power emitted from an assembly of electrons, we must convolve the power spectrum with the electron energy distribution and integrate over the electron velocity. However, since the recombination radiation is quantized by n and lacks a continuum to sum over, we can write the recombination radiation contribution simply as

$$4\pi\epsilon(\nu) = P_n 4\pi v^2 \frac{dv}{d\nu}, \tag{2.30}$$

Rearranging our expression for the radiation spectrum gives an alternate form for the electron velocity in terms of the emitted photon energy and energy level of the final

25

bound state.

$$v = \frac{2}{m}(h\nu - \frac{Z^2 R_y}{n^2})$$ (2.31)

Substituting this back into 2.30, the emissivity of the recombination radiation is then

$$\epsilon(\nu) = \frac{A}{4\pi} n_e \sqrt{\frac{m_e}{2\pi kT}} e^{\frac{-h\nu}{kT}} \left[\frac{2Z^2 R_y}{kTn^3} g_n(h\nu) e^{Z^2 R_y/n^2 kT} \right],$$ (2.32)

2.1.3 Combined Bremsstrahlung and Recombination Radiation Emissivity

Comparing the emissivities from recombination and bremsstrahlung radiation, the two emissivities have the same physical dependences. We can then set them equal up to a constant [14].

$$\epsilon(\nu)_{recomb} = \epsilon(\nu)_{brems}(\gamma - 1)$$ (2.33)

here the quantity $(\gamma - 1)$ is equal to the term in square brackets in 2.32. Since the total intensity of the continuum is $I = I_{brems} + I_{recomb}$, the factor γ describes what portion of the continuum comes from recombination radiation. This term is called the x-ray enhancement factor and its behavior explains the finite steps in the continuum from recombination radiation. As shown in 2-1, the continuum exhibits a series of edges. Since there is a minimum photon energy from recombination corresponding to an incoming electron at rest, the recombination radiation will exhibit a series of steps at energies defined as the recombination edges. For increasing temperatures, γ grows smaller as more electrons are ejected from bound states in ions and the contribution from bremsstrahlung grows greater. Comparing the recombination radiation intensity to our previous expression for the bremsstrahlung intensity, we can express the combined emissivity of the power radiated from bremsstrahlung and recombination
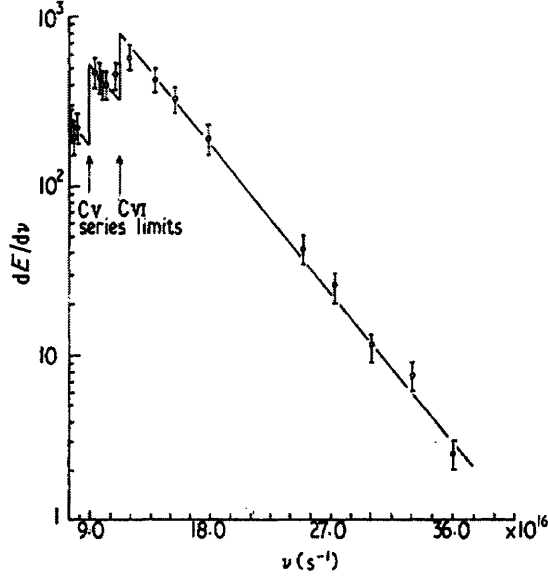
Figure 2-1: Combined bremsstrahlung and recombination radiation spectrum from carbon (after [15])

as

$$\epsilon(\nu) = \frac{A}{4\pi} n_e \sqrt{\frac{m}{2\pi kT}} e^{\frac{-h\nu}{kT}} \left(g_{ff} + \frac{2Z^2 R_y}{kTn^3} g_n(\nu) e^{Z^2 R_y/n^2 kT} \right) \qquad (2.34)$$

Radiative recombination varies more strongly with atomic charge than bremsstrahlung. For recombination radiation, we have $\epsilon \propto Z^4$ while bremsstrahlung power varies only as Z^2. This result agrees with our conceptual picture of recombination radiation; higher-Z impurities should more strongly attract electrons into bound states and thus recombination radiation should be stronger in Z than bremsstrahlung.

We can write the combined bremsstrahlung and recombination radiation in terms of a modification of the gaunt factor. The new combined gaunt factor is then [1]

$$g = g_f f + f_i(T, h\nu) \qquad (2.35)$$

$$f_i(T, h\nu) = 2\theta_i \sum_{n=m_i(h\nu)}^{\infty} \frac{e^{\theta_i/n^2}}{n^3} g_n(\nu), \qquad (2.36)$$

$$\theta_i = \frac{Z^2 R_y}{kT} \qquad (2.37)$$

27

The expression is summed from the lowest quantum number $n = m_i(h\nu)$ which corresponds to the lowest energy level the electron can be bound to and still emit a photon of energy $h\nu$. We define this level as

$$m_i(h\nu) - 1 < (\frac{h\nu}{Z^2 R_y})^{1/2} < m_i(\nu) \tag{2.38}$$

The exponential factor θ_i in the expression for $f_i(T, h\nu)$ determines the relative strength of the contribution from recombination radiation. For a typical electron temperature of a few keV, the contribution from recombination with the major constituents of the plasma (deuterium and helium) is negligible as $\theta_i \approx 10^{-3}$. However, for impurities with $Z > 10$ we have θ greater than 1 and recombination radiation becomes a major contributer to the plasma radiation continuum.

Finally, summing over all impurity species gives the total emissivity from free electron interactions.

$$\epsilon(\nu) = \frac{8\pi Z_{eff}^2 n_e^2}{3\sqrt{3}m_e^2 c^3} \left(\frac{e^2}{4\pi\epsilon_0}\right)^3 \sqrt{\frac{m_e}{2\pi kT}} e^{-h\nu/kT} \sum_i (g_{ff} + f_i) \tag{2.39}$$

$$Z_{eff} = \sum_i \frac{n_i Z_i^2}{n_e} \tag{2.40}$$

where we define an effective charge Z_{eff} that is characteristic of the entire plasma.

2.1.4   Profile Effects

With the expression for the combined bremsstrahlung and recombination emissivity, we may calculate the total photon flux incident upon the detector. Emissivity is defined as power per unit frequency volume solid angle. The differential form is

$$d\epsilon(\nu) = \frac{dP}{dV d\Omega d\nu} \tag{2.41}$$

We know that the detector subtends a solid angle $\Delta\Omega$. Multiplying through by $\frac{\Delta\Omega}{h}$ gives

$$\frac{\Delta\Omega}{h}d\epsilon(\nu) = \frac{dP}{dVd(h\nu)} \tag{2.42}$$

The incident power comes through a flux of N photons per second, each with an energy of $h\nu$. Substituting in $dP = h\nu dN/dT$ we have

$$\frac{\Delta\Omega}{h}\epsilon(\nu) = \frac{h\nu}{d(h\nu)}\frac{dN/dt}{dV} \tag{2.43}$$

To simplify the problem, we may assume that the plasma cross section is circular. Since the detector views the plasma through a chord of cross section dA, we can replace the volume element with $dV = dAdl$. Here l is the length of the chord that the detector sights along. The variable l is related to the toroidal parameter r by $l^2 = r^2 - d^2$ where d is the distance from the chord to the center of the torus. The above relation becomes

$$\frac{\Delta\Omega}{h}\epsilon(\nu)dl = \frac{h\nu}{d(h\nu)}\frac{dN/dt}{dA} \tag{2.44}$$

The left hand side is the differential photon flux incident upon the detector from a region of the plasma of thickness dl and cross sectional area dA. If we integrate over l, the total photon flux in units of photons $/(\text{second cm}^2)$ is

$$I(\nu) = \frac{\Delta\Omega}{h}\int_0^L \epsilon(\nu)dl \tag{2.45}$$

Following [1], we may calculate the incident photon flux by taking representative functions for the parameters in 2.45 and performing the integration. Taking a parabolic density profile, we may write $n_e(l)$ as

$$n_e(l) = n_0(1 - \frac{r^2}{a_l^2}) = n_0(1 - \frac{l^2 + d^2}{a_l^2}) \tag{2.46}$$

where n_0 is the central plasma electron density and a_l is the limiter radius. The temperature profile is assumed to be Gaussian and vary as

$$T(l) = T_0 e^{-r^2/a^2} = T_0 e^{-(l^2+d^2)/a^2} \qquad (2.47)$$

where a is the characteristic width of the temperature profile.

For a clean, hydrogenic plasma we have $Z_{eff} = 1$ and $n_i(l) = n_e(l)$. Using the approximation $g_{ff}(l) = (h\nu/kT(l))^{1/3}$ and assuming that recombination radiation is negligible for a hydrogenic plasma, 2.45 takes the form

$$I(\nu) = \frac{A\Delta\Omega}{4\pi h} \int_0^L n_e(l)^2 \sqrt{\frac{m_e}{2\pi k T(l)}} e^{\frac{-h\nu}{kT(l)}} \left(\frac{h\nu}{kT(l)}\right)^{\frac{1}{3}} \qquad (2.48)$$

Inserting the functions gives

$$I(\nu) = \frac{A\Delta\Omega}{4\pi h} n_0^2 \sqrt{\frac{m}{2\pi kT_0}} \left(\frac{h\nu}{kT_0}\right)^{\frac{1}{3}} e^{\frac{-h\nu}{kT_0}} \int_0^L (1 - \frac{l^2+d^2}{a_l^2}) \exp(\frac{5(l^2+d^2)}{6a^2} + \exp(\frac{l^2+d^2}{2a^2})) dl$$

The integration contains terms only dependent on the geometry of the detector and will be constant between shots. Since the PHA is only concerned with the relative itensities of the emission, we may absorb the integration into a constant. Dropping all terms that are constant between shots yields an expression for the relative photon flux incident upon the detector face

$$I(\nu) \propto Z^2 n_0^2 \frac{1}{\sqrt{kT_0}} \left(\frac{h\nu}{kT_0}\right)^{\frac{1}{3}} \exp(\frac{-h\nu}{kT_0}) \qquad (2.49)$$

2.1.5   Temperature Measurement

By measuring the relative bremsstrahlung intensity we can easily come to the central electron temperature. Taking the logarithm of 2.49 gives

$$\log I(\nu) \propto -\frac{h\nu}{kT_0} + \frac{1}{3}\log(\frac{h\nu}{kT_0}) - \frac{1}{2}\log(kT_0) + \log(Z^2 n_e^2) + I_0 \qquad (2.50)$$

30

where I have lumped together all the constants into the factor I_0. For temperatures above $R_y = 13.59eV$ and $h\nu \geq kT$ the term $\frac{h\nu}{kT_0}$ dominates the spectrum.

A semi-log plot of the intensity of the bremsstrahlung radiation against the energy of the detected x-rays will give a straight line with the slope inversely proportional to the electron temperature. Measurement of the bremsstrahlung spectrum will then be our primary method of determining the central electron temperature. This measurement is somewhat complicated by the presence of recombination radiation which will in practice be measured alongside the thermal bremsstrahlung. As shown for carbon in 2-1, the discontinuous recombination edges will distort the thermal bremsstrahlung continuum and must be cut out during analysis.

2.1.6   Bound Electron Interactions

In addition to the free-free and free-bound electron interactions that are responsible for the thermal continuum, electrons may transition between bound energy states. The simplest case for line radiation is a hydrogenic atom. We may quantize the electron energy levels using the Bohr model.

$$E_i = Z_i^2 \frac{R_y}{n^2} \tag{2.51}$$

An electron transition between two levels, n_1 and n_2, will then give emit a photon with wavelength given by the Rydberg formula

$$\frac{hc}{\lambda} = Z_i^2 R_y \left(\frac{1}{n_2^2} - \frac{1}{n_1^2} \right) \tag{2.52}$$

Using this formula, we can make a first approximation to the range of impurities species viewable by the detector. The energy range of the detector is from about 1 keV up to 30 keV. The strongest line radiation should come from K-alpha emission due to electron transitions from the innermost K shell to the second L shell. We can make the approximation that the remaining electron in the K shell will screen the nuclear charge giving an effective charge of $(Z - 1)$. Using the Rydberg formula,

an energy range of 1-30keV corresponds to K-alpha radiation from elements with $10 < Z < 55$. Many constituents of the the plasma facing components fall into that range. Line radiation is expected from Al, S, Cl, As, Ti, Cr, Fe, Ni, Cu and Mo.

Radiative Transitions and the Einstein Coefficients

We may describe the emission of photons from bound electron transitions in terms of the Einstein coefficients. For simplicity, consider a collection of a single impurity species with two bound electron states. The lower state has a wave function $|\psi_1 >$ and the upper state is $|\psi_2 >$. The total impurity density is n_i with n_1 of the atoms in the lower state and n_2 in the upper energy state.

There are three different processes by which an electron may transition between the two states. An electron initially in the upper state may spontaneously decay into the lower state and emit a photon. If we assign this process a rate coefficient A_{21}, the total rate of spontaneous decay is given as $n_2 A_{21}$. Similarly, an electron in the lower state may absorb a photon and be promoted to the higher state. The transition rate for this process is described by another coefficient $B_{12} I(\nu)$ where $I(\nu)$ is the energy density of the electric field of the absorbed photon. The upward transition rate is then $n_1 B_{12} I(\nu)$ Finally, an electron in the upper state may absorb a photon and undergo stimulated emission. The rate coefficient for this process is $B_{21} I(\nu)$ and the downward transition rate is $n_2 B_{21} I(\nu)$.

For the atoms to be in thermal equilibrium, the total upward transition rate must be balanced by the downward rate of transitions. We can write this balance as

$$n_2 A_{21} + n_2 B_{21} I(\nu) = n_1 B_{12} I(\nu) \qquad (2.53)$$

Denoting the energy of the two states as E_1 and E_2, a downward transition releases an energy

$$h\nu_{21} = E_2 - E_1 \qquad (2.54)$$

At a temperature T, the number ratio of the two states is then

$$\frac{n_1}{n_2} = \frac{e^{-(E_1/kT)}}{e^{-(E_2/kT)}} = e^{h\nu_{12}/kT} \tag{2.55}$$

Solving the balance equation for $I(\nu)$ gives

$$I(\nu) = \frac{A_{21}}{e^{h\nu_{12}/kT}B_{12} - B_{21}} \tag{2.56}$$

At thermal equilibrium we may take the electromagnetic energy density to be given by the Planck radiation formula.

$$I(\nu) = \frac{4h\nu^3}{c^3(e^{h\nu/kT} - 1)} \tag{2.57}$$

Comparing these two expressions for $I(\nu)$, we must have $B_{12} = B_{21}$ and A_{21} given as

$$A_{21} = \frac{8\pi h\nu_{21}^3}{c^3}B_{21} \tag{2.58}$$

Using this rate coefficient, the emission coefficient for spontaneous emission from this single transition is

$$\epsilon(\nu_{21}) = \frac{h\nu_{21}}{4\pi}n_2 A_{21}\phi(\nu_{21}), \tag{2.59}$$

where $\phi(\nu_{21}$ is the line emission profile. While atomic transitions have very well defined energies, the uncertainty principle and perturbations to the energy levels broaden the emission profiles away from delta functions. To calculate the emission coefficient from line radiation we will need an expression for the emission profile.

Emission Profiles

In the absence of broadening effects the profile from line emission would be sharply centered around the transition frequency. The emission profile would be very well described by a delta function. However, perturbations to the energy levels from

quantum effects, observation effects, and interactions with other atoms spread out the emission profile. The two main broadening effects are natural broadening from the uncertainty principle and Doppler broadening from the motion of the particles in the plasma. The electric fields from nearby particles tends to perturb the energy levels of the emitter through strak broadening. However, these effects are expected to be too small to measure with the PHA detector.

Natural Line Broadening

The mean lifetime of the excited state determines the natural width of the line emission profile. The Einstein coefficients are defined in terms of transition probabilities expressed in transitions per unit time. It follows that the lifetime of the excited state $|\psi_2>$ is inversely proportional to the transition rate.

$$\frac{1}{\Delta t} = A_{21} \tag{2.60}$$

The uncertainty principle gives the relation between the lifetime of the excited state and the measurable spread in the energy of the line radiation.

$$\Delta E = \frac{\hbar}{\Delta t} \tag{2.61}$$

The natural width of the line emission profile will then be

$$\Delta \nu = \frac{1}{2\pi \Delta t} \tag{2.62}$$

For the electrons in the excited state, the decay to the ground level is described in terms of an exponential function

$$n_2(t) = n_2(0)e^{-t/\Delta t} \tag{2.63}$$

so that the fraction of atoms in the excited state at time t is given as $e^{-t/\tau}$. Performing a Fourier transform on this quantity yields the fraction of ions in the excited state as

a function of the frequency.

$$f(\nu) = \frac{2}{\sqrt{2\pi}} \int_0^\infty e^{-t/\Delta t} e^{-2\pi i\nu t} dt \qquad (2.64)$$

Evaluating this integral gives the familiar Lorentzian distribution centered around the spontaneous transmission at ν_K

$$f(\nu) = \frac{1}{\pi} \frac{1/2\pi\Delta t}{(1/2\pi\Delta t)^2 + (\nu)^2} \qquad (2.65)$$

where $f(\nu)$ is normalized so that $\int_{-\infty}^\infty f(\nu)d\nu = 1$. Finally, convolving the fractional distribution of the energy states with the delta function model of the line emission gives the line emission profile due to natural broadening.

$$\phi(\nu) = \frac{1}{\pi} \frac{\Delta\nu}{(\Delta\nu)^2 + (\nu - \nu_{21})^2} \qquad (2.66)$$

Doppler Broadening

In addition to the natural broadening from the uncertainty in the energy, a broadening is introduced from the Doppler shift caused by the motion of the particles in the plasma. For non-relativistic motion, the Doppler shift in the frequency ν_{21} due to the particle velocity v along the line of sight of the detector is

$$\Delta\nu = \frac{v\nu_{21}}{c}, \qquad (2.67)$$

For the thermal particles in the plasma, the velocity distribution will be Maxwellian. The fraction of atoms with velocity in the range v to $v + dv$ with respect to the detector is then

$$f(v)dv = \sqrt{\frac{m}{2\pi kT}} \exp(\frac{-mv^2}{2kT})dv, \qquad (2.68)$$

where m is the mass of the emitter ion at temperature T. Writing $\Delta\nu = \nu_{21} - \nu$ and solving for v in 2.67 gives the particle velocity in terms of the shifted frequency.

$$v = (1 - \frac{\nu}{\nu_{21}})c \tag{2.69}$$

Finally, substituting the above expression into 2.68 and convolving with the initial assumption of a delta function emission profile gives the Doppler broadened line emission profile in terms of frequencies. The distribution is thus a Gaussian centered at the transition frequency ν_{21}

$$\phi(\nu) = \sqrt{\frac{m}{2\pi kT}} \exp(\frac{mc^2}{kT} \frac{(\nu_{21} - \nu)^2}{2\nu_{21}^2}) \tag{2.70}$$

For hydrogenlike argon at 3.7 $\mathring{A}$, the lifetime of the excited state has been measured as 3.54×10^{-9} s [16]. The line broadening from the uncertainty principle is on the order of 10^{-6} eV and negligible to the PHA.

Ion Temperature Measurement

Measurements of line radiation will encounter both Doppler and natural broadening. The combined effects of these broadening mechanisms will be to create a new emission profile. The convolution of the Lorentzian and Gaussian is a Voigt profile. Doppler broadening is expected to dominate over the natural line width. The measured line shape should be approximately Gaussian.

We may arrive at an estimate of the ion temperatures by measuring the FWHM of the Doppler broadened energy distributions. The FWHM of the Doppler energy distribution is given as

$$h\Delta\nu_{1/2} = 2\sqrt{2\ln(2)}\sqrt{\frac{kT}{mc^2}}h\nu_{21} \tag{2.71}$$

olving for the temperature gives

$$kT = \frac{mc^2}{8\ln(2)} \frac{(h\nu_{1/2})^2}{(h\nu)^2} \tag{2.72}$$

36

For a typical ion temperature on the order of 1 keV and a transition energy of 10keV, the Doppler broadened width will be on the order of 1 eV. Unfortunately, the overall resolution of the detector is two orders of magnitude higher. Ion temperature diagnostics have traditionally used crystal spectrometers [17]. While measuring Doppler shifts is out of reach for the current PHA system, future advances in detection equipment should make ion temperature measurement a goal for subsequent PHA systems.

Combined Line Emission Profile

As stated before, Doppler broadening is expected to dominate over the natural line width. However, the Doppler width is much smaller than the resolution of the detector. Since the broadening is too small to be recorded by the detector, we may discount line broadening and treat the line emission profiles incident on the detector as delta functions. The main source of broadening will come within the detector itself. Thus the emissivity that the detector see will be simply

$$\epsilon(\nu_{21}) = \frac{h\nu_{21}}{4\pi} n_i A_{21}, \qquad (2.73)$$

2.1.7 Impurity Line Radiation

If we assume the plasma is in coronal equilibrium, ions are promoted to excited states by collisions with free electrons and downward transitions occur through spontaneous emission. Here, I present the simpler case of collisional excitation. This occurs when a free electron collides with an ion and promotes a bound electron to a higher state. The excited bound electron then transitions downwards, emitting a characteristic photon. We can arrive at an estimate of the emissivity from collisional excitation by means of the Einstein coefficients.

Collisional Excitation

To calculate the emissivity of the line radiation we must first calculate the cross section for excitation. For monoenergetic electrons, a collection of n_1 ions in the

lower energy state sees an incoming flux of $n_e v$ electrons. For an interaction cross section σ_{12}, the total reaction rate per unit volume is then

$$R_0 = n_e v n_1 \sigma_{12} \tag{2.74}$$

Extending this to a Maxwellian population of thermal electrons, we must take the velocity average of the reaction rate.

$$R = <R_0> = n_e n_1 \int_{v_0}^{\infty} \sigma_{12} v f(v) d^3 v, \tag{2.75}$$

Here the lower limit of integration is the velocity v_0 which corresponds to the incoming electron having just enough energy to excite the bound electron to the next state. The minimum velocity is defined as $1/2 m v_0^2 = h \nu_{12}$.

With the line emission profile defined, we return to our expression for the emissivity 2.73. For an optically thin plasma, downward transitions from stimulated emission can be taken as negligible. We can then rewrite the balance equation as

$$n_2 A_{21} = n_1 B_{12} I(\nu) \tag{2.76}$$

Since the collisional excitation rate is specified in 2.75, we can set $R = n_e n_1 B_{12} I(\nu)$ or

$$A_{21} = n_e \frac{n_1}{n_2} \int \sigma_{12} v f(v) d^3 v \tag{2.77}$$

At temperature T, the ratio of the density of ions in each state is

$$\frac{n_1}{n_2} = \exp(\frac{-E_{12}}{kT}) \tag{2.78}$$

For an optically thin plasma with a single two-state ion, in terms of the interaction

cross section, the emissivity is

$$\epsilon(\nu) = \frac{h\nu_{12}}{4\pi} n_e n_i \exp(\frac{-h\nu_{12}}{kT}) \int_{v_0}^{\infty} \sigma_{12} v f(v) d^3v, \qquad (2.79)$$

Following [6], we can arrive at a semi-classical estimate of the collisional excitation cross section by approximating the electron-ion system as an electric dipole. For collisional excitation, we can treat the perturbing electric field of the colliding electron in very much the same way as we did for bremsstrahlung radiation. A collision between a free electron and an ion has a certain chance of inducing an electron transition that is related to the Einstein coefficient B_{12}. The interaction cross section is

$$\sigma_{12} = B_{12} \frac{8\pi}{\sqrt{3}} \frac{R_y a_0}{v^2} G \qquad (2.80)$$

where a_0 is the Bohr radius, v is the velocity of the incoming electron, and G is the usual Gaunt factor which encapsulates the quantum mechanical corrections. Continuing our assumption of an electric dipole and dropping higher order contributions, the transition probability B_{12} can be written in terms of the dipole moment of the system [18].

$$B_{12} = \frac{4\pi^2 e^2}{3\epsilon_0 \hbar^2 c} | <\psi_2|\vec{r}|\psi_1> |^2 \qquad (2.81)$$

here the quantity $| <\psi_2|\vec{r}|\psi_1> |^2$ is the the square of the magnitude of the dipole moment for the transition and $\vec{r}$ is the sum of the position vectors of the all of the interacting electrons.

For hydrogenic ions, we can easily calculate the magnitude of the transition dipole moment. The heavier impurities in the plasma will only be partially ionized. Calculations of the transition dipole moment must take into account the complex interactions between the transitioning electron and the rest of the bound electrons in the ion. In addition, screening effects must be included to account for the fact that each electron only sees a portion of the nuclear charge. The matrix elements for the transition dipole

moment for heavier ions are not well described analytically and must be measured empirically.

We can express the cross section given in 2.80 in terms of classical oscillators. We define the classical oscillator strength f_{12} as the ratio of the number of classical oscillators to the number of ions in the upper level. For states that are weak emitters, transitions occur infrequently and the ion can be treated as a state of relatively few oscillators so $f_{12} \to 0$. Conversely, strong transitions oscillate more readily and so nearly all the electrons may be modeled as oscillators, $f_{12} \to 1$. This ratio is given in terms of the Einstein coefficients as

$$f_{12} = \frac{4\pi\epsilon_0}{e^2}\frac{m_e}{\pi}h\nu_{12}B_{12} \qquad (2.82)$$

The oscillator strengths are generally well known from empirical measurement and are compiled by NIST. Using oscillator strengths in our calculations is advantageous because they are unit-less quantities. Unlike the Einstein coefficients, oscillator strengths merely describe the strength of the transition.

In terms of classical oscillators the cross section in 2.80 is then

$$\sigma_{12} = 4\pi^2 a_0 \frac{e^2}{4\pi\epsilon_0} \frac{R_y}{1/2m_e v^2} \frac{R_y}{h\nu_{12}} f_{12} \frac{\pi G}{\sqrt{3}} \qquad (2.83)$$

Which we can rewrite to recover the form originally given by van Regemorter [19] as

$$\sigma_{12} = \frac{8\pi}{\sqrt{3}}\pi a_0^2 f_{12} \frac{R_y^2}{(h\nu_{12})^2} \frac{(h\nu_{12})}{1/2m_e v^2} G(v) \qquad (2.84)$$

The emission rate is then

$$R = \frac{64\pi^3 a_0^2 R_y^2}{m^2 h\nu_{12}} f_{12} \sqrt{\frac{m}{2\pi kT}} \exp\left(\frac{-h\nu_{12}}{kT}\right) \int_{v_0}^{\infty} \exp(\frac{-mv^2}{2kT})vG(v)dv \qquad (2.85)$$

Taking the Gaunt factor as small, we can perform the integration in the classical

limit. The integration yields

$$R = \frac{64\pi^3 a_0^2 R_y^2 n_e}{h\nu_{12}m} \sqrt{\frac{m}{2\pi kT}} kT f_{12} \exp\left(\frac{-mv_0^2}{2kT}\right) \qquad (2.86)$$

The total emissivity is

$$\epsilon(\nu_{12}) = \frac{16\pi^2 a_0^2 R_y^2}{m^2} \sqrt{\frac{m}{2\pi kT}} f_{12} kT n_i n_e \exp\left(\frac{-2h\nu_{12}}{kT}\right) \qquad (2.87)$$

Dropping the constants yields the overall temperature dependence of the emissivity

$$\epsilon(\nu_{12}) \propto n_i f_{12} \exp\left(\frac{-2(h\nu_{12})}{kT}\right) \sqrt{kT} \qquad (2.88)$$

For a given transition, the emissivity is exponential for low temperatures and goes as $\sqrt{T}$ for $kT > h\nu_{12}$.

The difficulty in measuring the throughput of the PHA system means that we cannot in general measure absolute emissivities. However, measurements of the line strength of each shot relative to a baseline will yield information on the relative impurity concentration. For each shot, we may use the the temperature found from measuring the electron bremsstrahlung radiation to factor out the temperature dependence of the emissivity. With the complicating effects of temperature factored out, the relative ion density can be determined by the ratio of the measured line strength to the baseline value.

Chapter 3

Detection and Signal Processing Apparatus

Alcator C-Mod is a compact, high field tokamak with a major radius of 68 cm and a minor radius of 22 cm. While the small size of C-Mod allows record high magnetic fields, the compactness makes ensuring all the diagnostics have a view of the plasma a rather difficult problem.

Ports on the outside of C-Mod allow for diagnostic access to the plasma. The soft x-ray PHA diagnostic views the plasma through K Port. The PHA viewing chord is nearly at the midpoint of the torus so the PHA sees a good portion of the central and edge effects. Since so many diagnostics are packed around the device, a long beam line was installed to carry the photons from the exit point at the K port flange to where there was space to fit the detector.

A block diagram of the experimental apparatus is given in Figure 3-1. The left most side indicates the connection to the K port flange. From the flange, a 2 3/4 inch stainless steel tube forms the beam line that carries the x-rays from the plasma. Approximately 65 inches along the beam line, a slit was installed to collimate the x-rays. From the pinhole aperture of the slit, the x-rays continue out another 60 inches until they encounter another collimating slit.

Since the beam line is in direct contact with the plasma, it is essential that the interior be held at vacuum. An ion pump was attached to ensure that the beam line

43
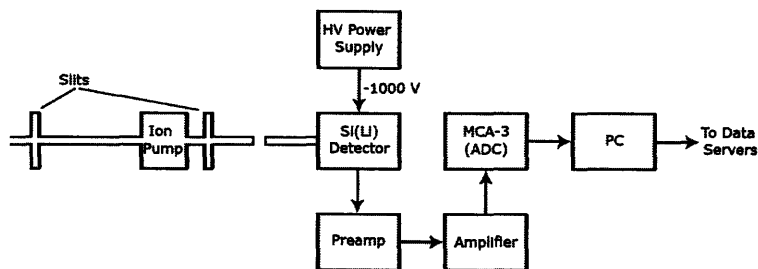
Figure 3-1: Block diagram of the apparatus.

stayed under vacuum. A convectron gauge provided measurement of the pressure inside the beam line and confirmation of the vacuum. Access to the plasma was controlled by a gate valve. After the beam line was pumped down and ensured to be at the correct pressure, the gate valve was opened to give a view of the plasma.

After the second slit, the x-rays exit the beam line and encounter the detector, an Ortec SLP series Si(Li) spectrometer. There is a small air gap between the end of the beam line and the entrance to the detector. This gap allows the insertion of beryllium foils to attenuate the signal. However, the air itself attenuates the x-ray signal and thus must be included in calculations of the attenuation from the beryllium filters. There is also an additional thickness of beryllium from the window of the detector. After the x-rays move into the detector, they encounter the crystal element.

The individual x-rays are converted to proportional electric pulses by the detector. The detector was biased with -1000 V from a Bertran high-voltage power supply. From the detector, the signal entered an Ortec Model 259 preamplifier. The amplified signal was then sent to a Canberra Model 2022 spectroscopy amplifier. The amplifier was set to an amplification factor of 300 and a shaping constant of 0.5 μs. From the amplifier, the signal was sent into the ADC input on the FAST Comtec MCA-3 multichannel analyzer card. The MCA-3 card contains an integral ADC and is mounted in a PC. Finally, the PC wrote each collected spectrum onto the main Alcator data servers.
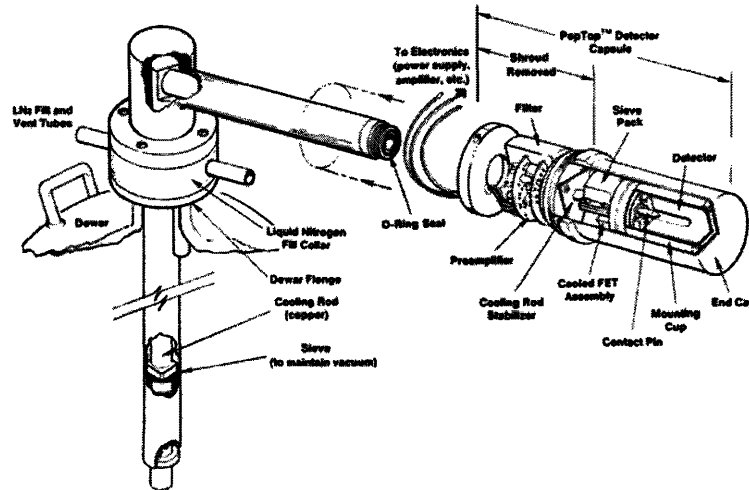
Figure 3-2: ORTEC SLP Silicon (Li) X-Ray Detector in PopTop Capsule. Adapted from [20]

3.0.8 Semiconductor Radiation Detectors

The Ortec SLP series soft X-ray detector consists of a high-purity, lithium-drifted silicon (Si(Li)) detector attached to an integral preamplifier. The detector and preamplifier are encapsulated in a PopTop capsule and are mounted to a liquid nitrogen dewar. The detector views through a thin attenuating beryllium window. A diagram of the detector and the supporting apparatus is given in Fig. 3-2.

When a photon enters the detector, it has a chance of interacting with one of the silicon atoms in the crystal. If a silicon atom absorbs the incoming photon, electrons may be promoted to an excited state and emit characteristic radiation. Alternatively, a valance electron may gather enough energy to make a jump to the conduction band in a process analogous to photoelectric absorption. The theoretical minimum energy resolution of the detector is set by the band gap energy ϵ of the crystal. If the incoming photon has energy $h\nu_i$, the emitted electron will then have a kinetic energy equal to $E = h\nu_i - \epsilon$.

The active region of the detector is sandwiched between a p-type and n-type region. Electrons liberated by photoelectric absorption are swept out of the detector by the bias voltage and enter into the signal processing chain.

45

Ion Drifting

The detection scheme described above requires that the active area of the detector is neutral with an equal concentration of positive and negative charge carriers. Otherwise, the prevailing charge carriers would dwarf the signal from incoming radiation. For the simple p-n diode discussed above, the neutral depletion zone is typically too small to interact with high energy radiation. A method to extend the neutral active area is needed to measure penetrating radiation.

Simply sandwiching a non-doped, intrinsically neutral region of silicon between the p and n-type areas of the diode would not work. The trace impurities present in high-purity silicon tends to make it weakly p-type. To restore the neutrality of silicon, electron donors must be introduced to balance the charge. Lithium ions are readily absorbed by silicon to form interstitial impurities. A process called ion drifting allows lithium to be introduced into the silicon crystal to balance the charge.

Ion drifting is the last stage of an intensive fabrication process to prepare the detector element. The prepared silicon crystal is heated and lithium is allowed to diffuse through one of the contact surfaces of the crystal. The thin surface region with the interstitial lithium content becomes n-type. The introduction of the lithium ions thus creates a p-n diode. A reverse bias is applied to the diode while the temperature is slowly elevated. The elevated temperature increases the mobility of the lithium ions while the electric field encourages the ions to drift further into the crystal. The ions stop drifting when the local electric field is net neutral; the number of positive charges from impurities is equal to the introduced negative charges from lithium. The lithium ions thus arrange themselves to balance perfectly the silicon crystal to create a wide neutral region that can more easily interact with high-energy radiation.

Particular care must be exercised when using a Si(Li) detector. As the drifting process was accomplished by reverse biasing the detector, operating the detector with a forward bias at room temperature will cause the lithium ions to drift back out of the compensated region. To keep the lithium ions from escaping, the detector must be cooled to cryogenic temperatures. At low temperatures, the thermal mobility of the

46
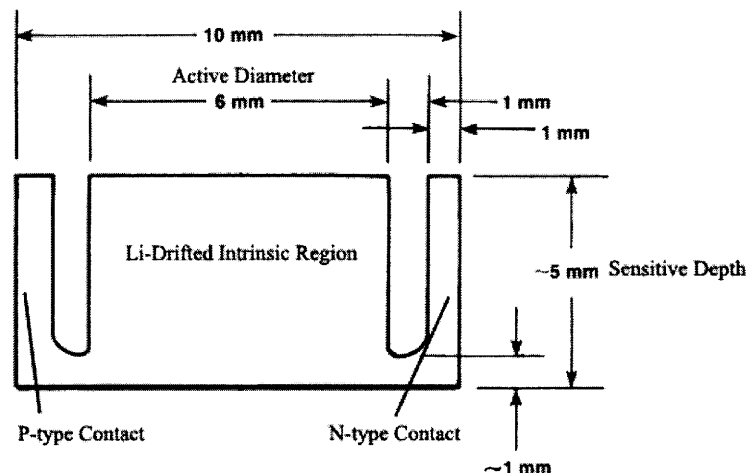
Figure 3-3: Diagram of Si(Li) detector element. Adapted from [20]

lithium ions is reduced to the point where the bias voltage does not dislodge them. A 30 L liquid nitrogen dewar is attached to the detector capsule for this purpose.

Detector Settings

An Ortec Model SLP-06180-P-S Si(Li) low-energy photon spectrometer was used to measure the energy of the incoming x-rays. A high voltage bias of -1000V was supplied to the detector. The power source was filtered by an Ortec 138L high voltage filter. The sealed PopTop capsule maintained a vacuum to eliminate attenuation effects from the air and protect the crystal. The FWHM of the detector was measured at 164eV for the 5.9 keV [55]Fe $K\alpha$ peak at an amplifier time constant of $10\mu s$.

A diagram of the crystal element is given in Fig.3-3. The silicon crystal was in a planar configuration with an active diameter of 6mm and a sensitive depth of 5.35mm. The active area of the detector was 28mm. The crystal was coated with two absorbing layers; a $0.02\mu m$ thick layer of gold and a $0.1\mu m$ thick layer of silicon. The detector viewed through a 0.0127 mm thick beryllium window.

3.0.9 Saturation and Pulse Pile-Up

The signal from the detector was fed into an Ortec Model 259 Pulsed-Optical-Feedback preamplifier in a charge sensitive configuration. The maximum usable counting rate

of the preamplifier is the limiting factor of the detector for measuring high intensity sources. The nominal limit for the preamplifier is an energy rate of 4000 MeV/s. For the soft x-rays observed, the counting limit of the preamplifier is then on the order of 400,000 counts/s.

However, the signal was observed to saturate at much lower counting rates, below 100,000 counts/s. This limit is attributable to the degradation of the signal baseline coming from the detector. The ADC in the MCA-3 depends on receiving Gaussian pulses from the amplifier. At higher count rates the baseline degrades making pulses more difficult to discern. Without a clear baseline, the ADC in the MCA-3 fails to register incoming pulses and the counting rate goes to zero.

A BNC BH-1 tail pulse generator was used to assess the limits of the usable count rate. The tail pulses were set to come in regularly with a rise time of $.02\mu s$ a fall time of $.05$ μs and a width of $10\mu s$. The shaping constant of the amplifier was set to $2\mu s$. As the counting rate increased above 100,000 counts/s, the waveform from the amplifier changed. After each pulse, the baseline became negative before refcovering a short time later. At rates approaching 200,000 counts/s, the baseline degraded to such a point that amplifier output no longer resembled Gaussian pulses, rather a waveform that resembled the merging of the Gaussians to form a sinusoidal wave train. At this point, the ADC in the MCA-3 did not see any of the expected Gaussian pulses from the amplifier. Although pulses were still entering the ADC from the amplifier, the ADC could not make any sense of them and the counting rate dropped to zero.

While this measurement further refined the upper limit of the counting rate, the true counting limit can only be assessed by introducing random pulses from an x-ray source. Slowly moving source towards the detector will increase the count rate until a precipitous drop occurs from saturation. Using a ^{55}Fe source yields the maximum usable count rate as 80,000 counts/s.

Photons normally enter the detector randomly spaced in time. When two photons enter the detector at nearly the same time, the resulting effect of pulse pile-up can degrade the signal. From the detector, the two pulses enter the amplifier and superimpose to form a combined signal. If two pulses of the same energy come into

the amplifier at the exact same time, the resulting combined pulse will have twice the amplitude and will be recorded by the MCA as having twice the energy. In reality, the amount of overlap of the two pulses is random. At high counting rates, pile-up will create a secondary false photopeak at twice the energy of the actual peak. In between the two peaks there will be a continuum from impartial overlap of the two pulses. Higher order peaks are also possible from the coincidence of more than two photons.

For an incoming photon to avoid pile-up, no other photons must enter the detector within one time interval of the amplifier. At a counting rate of r and an amplifier time constant of μ, the probability of observing a time interval greater than μ is given as [21].

$$P(> \mu) = \exp(-r\mu) \tag{3.1}$$

The probability of two pulses piling up is then $P(> \mu)^2$. For a counting rate of 80,000 and an amplifier shaping constant of 2μs, the probability of pulse pileup is about 30 percent. Pileup may be avoided by decreasing the shaping constant of the amplifier at the expense of energy resolution. As energy resolution isn't critical to the PHA, a low time shaping was chosen to maximize performance at high count rates.

3.0.10   Attenuation Filters

To reduce the counting rate from the plasma to a measurable range, beryllium filters were introduced into the beam line. Beryllium is particularly opaque to soft x-rays and so makes an excellent attenuator. The attenuation from the beryllium filters is dependent on the energy of the incoming photons. The filtered signal thus takes on a line shape from the filters that must be subtracted from the signal.

A collimated beam of photons with initial intensity I_0 is incident upon a filter of thickness l. The emerging intensity is then given by

$$I = I_0 \exp(-\frac{\mu}{\rho}l) \tag{3.2}$$

49
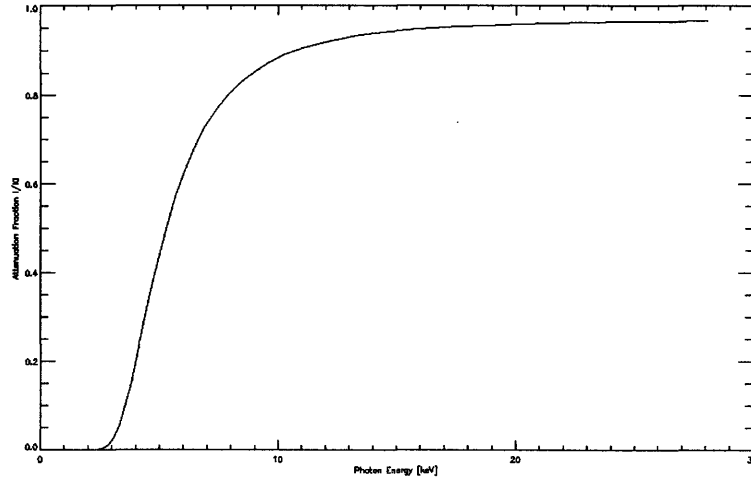
Figure 3-4: Fractional intensity of X-rays against incident energy for attenuation through a 1 mm Be foil and 2 cm of air. Data from NIST [22]

The factor $\frac{\mu}{\rho}$, or the mass attenuation coefficient, is a well known coefficient for each element and is compiled by NIST. For a series of n absorbers, the above equation takes the form

$$I = I_0 \exp(-\sum_i^n \frac{\mu_i}{\rho_i} l_i) \tag{3.3}$$

where $\frac{\mu_i}{\rho_i}$ and l_i are the attenuation coefficients and thicknesses of the ith absorber. For a beryllium filter and an air gap, the attenuation is simply the sum of the effects from the beryllium and the constituents of the air. For a typical air gap and filter thickness, a plot of the fractional intensity I/I_0 is given in Figure 3-4.

3.1 MCA Interface

The shaped and amplified pulses from the detector were then fed into a FAST Comtec MCA-3 multichannel analyzer. The MCA formed the interface between the signal detection electronics and the signal analysis software. The MCA operated as a PCI card mounted in a PC running Microsoft Windows XP. The operation of the MCA was controlled by the provided MCA interface software.

While the MCA interface software provided local control over the operation of the

MCA, an external software interface was needed to automate the data acquisition process. Instead of responding to local user input, the FastComtec MCA interface software was rewritten to respond to automated control from the main MDSplus tree. Developing the automation process was not without difficulty as the MCA card only supported systems running Microsoft Windows and the main computing environment at C-Mod is Linux based.

At the start of a plasma shot, the MDSplus tree executed the PHA initialization node. User defined configuration values were read from the MDSPLUS tree and the configuration file was written to a directory on the PC. As the low-level MCA driver interface was not responsive to configuration changes, a command was sent to the PC to crash the MCA interface and reload the program. With the configured MCA ready to take data, the next signal from the PHA branch of the MDSplus tree created a dummy file in a local directory. The MCA interface software searched for the presence of this file. When the file was present, the MCA was instructed to begin collection of data and delete the dummy file. The final step came after a closing signal from the MDSplus tree. The completed data set was written to the MDSplus tree and the MCA software interface was reset.

3.1.1 MCA Settings

Some typical values for the MCA-3 configuration file are given here. The lower level discriminator was set to 150 channels, the range was set to collect over the full 8192 channels. Each spectrum was time integrated with a live time preset of 10ms. The time integration was repeated 128 times to capture the full plasma discharge. An option in the configuration file allowed for collection of additional cycles of 128 time intervals each. Adjustment of the live time preset required that the number of cycles be changed accordingly to cover the enitre discharge.

The MCA-3 was configured to separate the collected spectrum into discrete time intervals. The available listmode in the MCA-3 configuration settings allowed the time integrated spectra to be laid seamlessly end to end in the MCA-3 onboard memory. The listmode operated as follows. After the trigger came to begin collection, the

MCA would collect data over the full range of 8192 channels for a user defined length of time, typically 10ms. After the first time interval was up, the MCA would move ahead in the memory by 8192 channels and begin writing the next spectrum. This process would repeat for a defined number of cycles, typically 128 to cover the entirety of the plasma shot.

The MCA-3 onboard memory contained a 2 megabyte SRAM chip organized as 512k channels each with a 32 bit capacity. The card was able to write spectra into the onboard memory buffer while simultaneously freeing capacity by dumping the old data into the main memory of the PC with no additional dead time penalty. The fast data processing of the MCA-3 card is critical to the time integration since the size of a typical spectrum collected in this way is in excess of 3 MB. This capability allowed for integration times tested down to below 1 ms.

Chapter 4

PHA Measurements

4.1 Energy Calibrations

The detector was calibrated using the photopeaks from a 50mCi [55]Fe source and a 5 mCi [241]Am source. The peaks in each spectrum were fitted to Gaussians and compared to the known energy of the transitions. The energy spectrum from the [241]Am source is given in Fig. 4-1. The combined calibration curve from the two sources is shown in Fig. 4-2. A least squares fitting to the data yielded the energy calibration of the detector.

Table 4.1: Reference transition energies

Peak	Emitter	Transition	Energy [keV]
1	^{55}Mn	K-L$_3$ (Kα_1)	5.90
2	^{55}Mn	K-M_3	6.50
3	^{58}Ni	K-L_3	7.48
4	^{58}Ni	K-M_3	8.26
5	^{237}Np	L$_3$−M$_1$	11.87
6	^{237}Np	L$_3$−M$_5$	13.94
7	^{237}Np	L$_3$−N$_1$	16.11
8	^{237}Np	L$_1$−M$_2$	17.06
9	^{237}Np	L$_2$−M$_4$	17.75
10	^{237}Np	L$_1$−N$_1$	20.83
11	^{241}Am	L$_2$−N$_2$	21.51
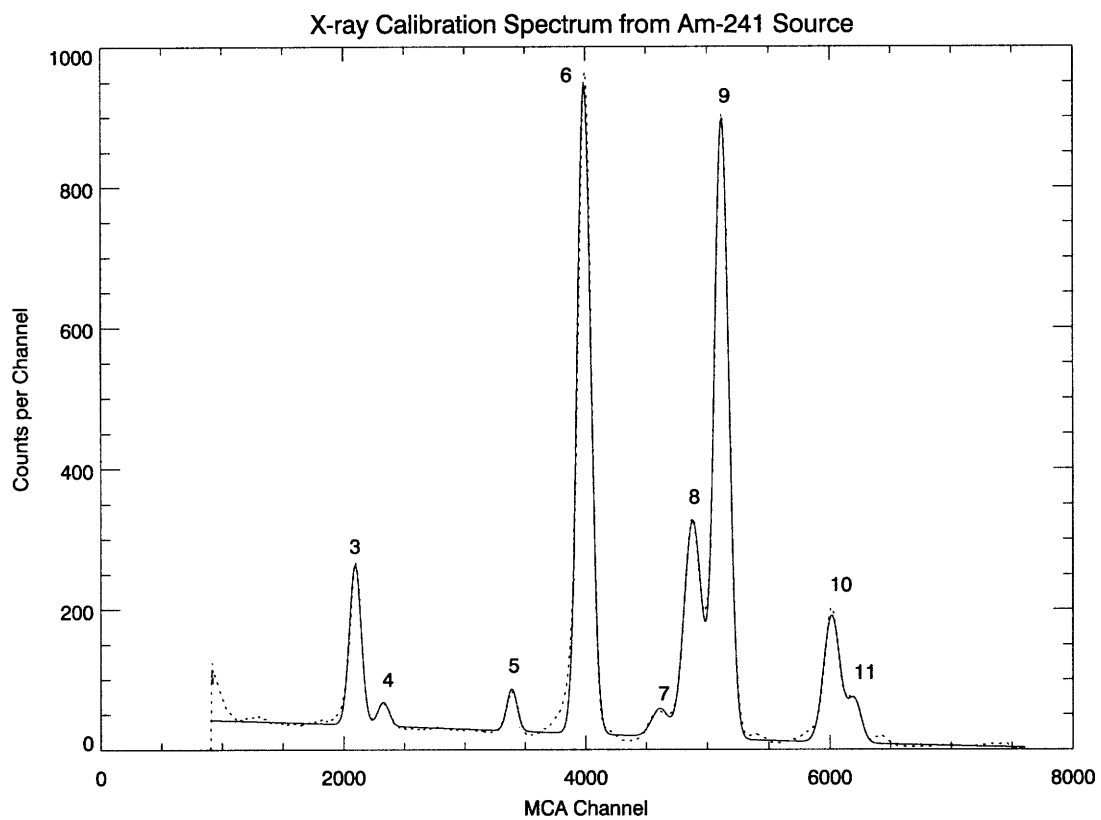
Figure 4-1: Calibration spectrum from ^{241}Am source. The dotted line is the raw spectra while the solid line is the calculated fit. The labeled photopeaks are summarized in Table 4.1
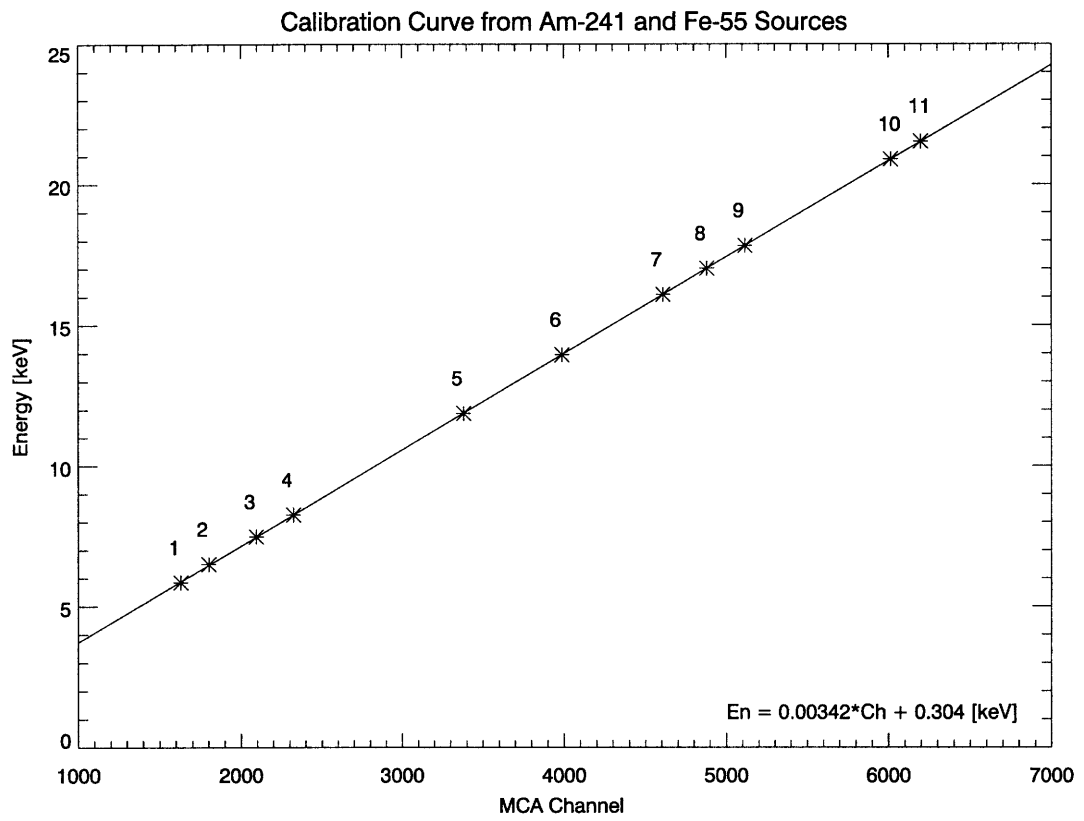
Figure 4-2: Calibration curve for detector apparatus with ^{55}Fe and ^{241}Am sources.

4.2 Plasma Measurements

A current limitation of the PHA system is that it doesn't behave predictably at very high count rates. During the 2006 campaign, a large amount of time was spent correcting the beryllium filters to allow the PHA to operate over an entire plasma discharge without saturating and shutting down measurement. While the problem was corrected by the end of the 2006 campaign, the PHA has system has not yet taken any data with the corrected filters. Preliminary measurements taken during calibration are available to assess the operation of the PHA. As the PHA shut down when the plasma reached peak emissivity, the photopeaks from impurity radiation are absent. However, determination of the line integrated electron temperature as proof of principle is possible.

A preliminary measurement of the thermal electron spectrum is shown in Fig. 4-3. The analysis gives an electron temperature of 2.06 keV. Distortion of the spectrum from recombination radiation at around 2 eV and 3 eV is evident in this part of the spectrum. However, there is insufficient resolution in the data set to identify the recombination edges.

4.3 Conclusion

The development of a soft X-ray pulse height analysis diagnostic system has been discussed. Measurements of the thermal electron bremsstrahlung radiation confirms the theoretical dependences of intensity on incident x-ray energy. A preliminary measurement of the electron temperature yields a value of 2.06 keV which is proof of the capabilities of the PHA system. A late start in the plasma run campaign and difficulties in installing the detector have frustrated efforts to perform more detailed tests of the PHA diagnostic. Identification of the plasma impurity radiation will be a task that is left to future researchers.
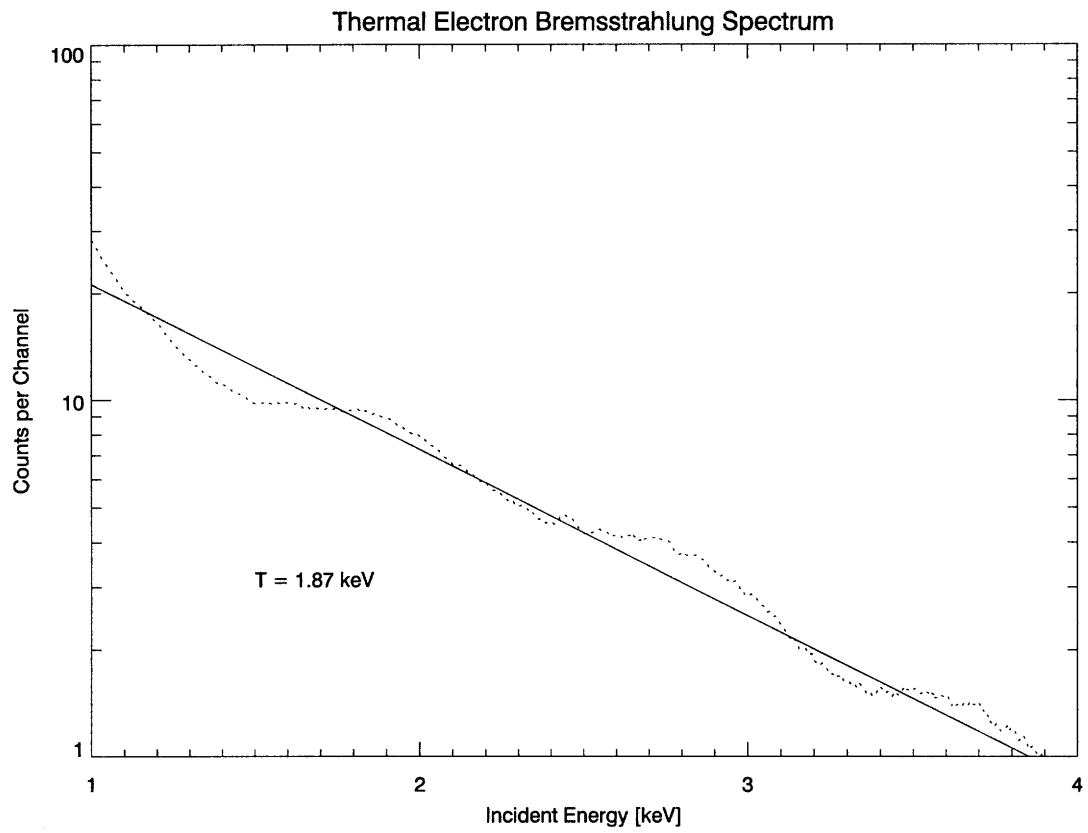
Figure 4-3: Thermal Electron Spectrum Recorded by the PHA system. The dotted line is the smoothed dataset and the solid line is the fit.

Bibliography

[1] J E. Rice, Kim Molvig, and Heikki I. Helava. Continuum x-ray emission from the alcator a tokamak. *Phys. Rev. A*, 25(3):1645–1668, Mar 1982.

[2] J. E. Rice and K. L. Chamberlain. X-ray observations between 10 and 150 kev from the alcator-c tokamak. *Phys. Rev. A*, 38(3):1461–1467, Aug 1988.

[3] D. Pasini, RD Gill, J. Holm, E. van der Goot, and A. Weller. Jet x-ray pulse-height analysis system. *Review of Scientific Instruments*, 59:693, 1988.

[4] Y. Shi, Z. Chen, B. Wan, B. Lv, L. Hu, S. Lin, Q. Hu, J. Qian, H. Liu, S. Liu, et al. Soft x-ray pulse height analyzer in the HT-7 tokamak. *Review of Scientific Instruments*, 75:4930, 2004.

[5] L.D. Landau and E.M. Lifshitz. *The Classical theory of fields*. Pergamon Press, Oxford, U.K.; Reading, U.K., rev. 2nd edition, 1962.

[6] I.H. Hutchinson. *Principles of Plasma Diagnostics*. Cambridge University Press, 2002.

[7] H.A. Kramers. *On the Theory of X-ray Absorption and of the Continuous X-ray Spectrum*. A. A. Knopf, New York, 1923.

[8] JA Gaunt. Continuous absorption. *Philosophical Transactions of the Royal Society of London. Series A, Containing Papers of a Mathematical or Physical Character*, 229:163–204, 1930.

[9] A. Sommerfeld and AW Maue. Approximate adaptation of a solution of the Schrodinger equation to the solution of Dirac's equation. *Ann. Physik*, 22:629–642, 1935.

[10] A. Sommerfeld. *Atombau und Spektrallinien*, volume II. Vieweg, Braunschweig,, 1939.

[11] D. H. Menzel and C. L. Pekeris. Absorption coefficients and hydrogen line intensities. *Monthly Notices of the Royal Astronomical Society*, 96:77, 1935.

[12] PJ Brussaard and HC van de Hulst. Approximation formulas for nonrelativistic bremsstrahlung and average gaunt factors for a maxwellian electron gas. *Reviews of Modern Physics*, 34(3):507–520, 1962.

[13] WJ Karzas and R. Latter. Electron radiative transitions in a coulomb field. *The Astrophysical Journal Supplement Series*, 6:167, 1961.

[14] K. Brau, S. von Goeler, M. Bitter, R. D. Cowan, D. Eames, K. Hill, N. Sauthoff, E. Silver, and W. Stodiek. Observations of giant recombination edges on the princeton large torus tokamak induced by particle transport. *Phys. Rev. A*, 22(6):2769–2775, Dec 1980.

[15] M. Galanti and NJ Peacock. Quantitative x-ray spectroscopy of the light-absorption region at the surface of laser-irradiated polyethylene. *Journal of Physics B: Atomic, Molecular, and Optical Physics*, 8(14):2427–2447, 1975.

[16] Robert W. Schmieder and Richard Marrus. Two-phonon decay and lifetime of the $2^2 s_{\frac{1}{2}}$ state of hydrogenlike argon. *Phys. Rev. Lett.*, 25(25):1692–1695, Dec 1970.

[17] E Källne, J Källne, E S Marmar, and J E Rice. High resolution x-ray spectroscopy diagnostics of high temperature plasmas. 31(6):551–564, 1985.

[18] H. Griem. *Plasma Spectroscopy*. McGraw-Hill, 1964.

[19] H. van Regemorter. Rate of collisional excitation in stellar atmospheres. *The Astrophysical Journal*, 136:906, 1962.

[20] Ortec Inc. Photon detectors. 2004. Date retrieved:May 15, 2007 http://www.ortec-online.com/electronics/amp/amplifiers.htm.

[21] GF Knoll. Radiation detection and measurement. *John Whiley and Sons, New York*, 1979.

[22] JH Hubbell and SM Seltzer. Tables of X-Ray Mass Attenuation Coefficients and Mass Energy-Absorption Coefficients from 1 keV to 20 MeV for Elements Z= 1 to 92 and 48 Additional Substances of Dosimetric Interest. Technical report, PB–95-220539/XAB; NISTIR–5632, National Inst. of Standards and Technology-PL, Gaithersburg, MD (United States). Ionizing Radiation Div., 1995.